Chemistry–A European Journal
Full Paper
doi.org/10.1002/chem.202101700
Chemistry Europe
European Chemical Societies Publishing

Magnesium Deintercalation From the Spinel-Type $MgMn_{2-y}Fe_yO_4$ ($0.4 \leq y \leq 2.0$) by Acid-Treatment and Electrochemistry

Alejandro Medina,[a] Ana I. Rodríguez,[a] Carlos Pérez-Vicente,[a] and Ricardo Alcántara*[a]

Abstract: Rechargeable magnesium batteries attract lots of attention because of their high safety and low cost compared to lithium batteries, and it is needed to develop more efficient electrode materials. Although $MgMn_2O_4$ is a promising material for the positive electrode in Mg rechargeable batteries, it usually exhibits poor cyclability. To improve the electrochemical behavior, we have prepared nanoparticles of $MgMn_{2-y}Fe_yO_4$. The XRD results have confirmed that when Mn^{3+} (Jahn-Teller ion) ions are replaced by Fe^{3+} (non-Jahn-Teller ion), the resulting $MgMn_{2-y}Fe_yO_4$ is a cubic phase. The structure and theoretical voltage are theoretically calculated by using the DFT method. The obtained samples have been chemically treated in acid solution for partial demagnesiation, and it is observed that the presence of iron inhibits the deinsertion of Mg through disproportionation and favors the exchange reaction. The electrochemical behavior in non-aqueous magnesium cells has been explored.

Introduction

High cost, scarcity of mineral resources and low volumetric capacity are some of the factors that can limit the application of lithium batteries to electric vehicles. As an alternative to lithium, the feasibility of rechargeable magnesium batteries should be thoroughly studied.[1] Besides the problematic of using Mg anode,[1a] another major hurdle is the lack of materials that undergo reversible (de)intercalation of magnesium.[2] Thus, the theoretical and experimental studies on the (de)intercalation of magnesium are relevant to develop the future magnesium batteries, although the low compatibility between the most common electrolyte solutions and Mg metal and many active materials is a major drawback for the proper experimental studies.[3]

Because of the structural stability and high voltage, the oxides with spinel-type structure AB_2O_4 are among the most promising electrode materials for magnesium batteries. On the contrary to some previous assumptions, recently it has been demonstrated that the migration of Mg^{2+} in spinel oxides is possible at acceptable rates, permitting electrode function at reasonable particle sizes, and this migration is sensitive to structural disorder within the spinel lattice.[4] Some calculations found that the theoretical voltage for demagnesiation of a spinel such as $MgCr_2O_4$ (up 4.2 V vs. Mg) is out of the stability of the common electrolyte solutions.[5] In addition, it is known that $MgClO_4$ in acetonitrile (ACN) solution blocks the surface of Mg electrode during the plating,[5] while magnesium bis (trifluoromethylsulfonyl)amide in dimethoxyethane (DME) can be oxidative decomposed during the charge of the battery. Besides that, the desolvation of magnesium can be particularly difficult for bidentate DME.[5]

One of the most promising materials for magnesium batteries is $Mg_xMn_2O_4$. If all the range of composition from $x=0$ (corresponding to Mn^{4+}) to $x=2$ (corresponding to Mn^{2+}) is deployed, its theoretical capacity is 616.6 $mAh\,g^{-1}$, but the experimental capacities that were reported are significatively lower. The use of the spinel-type $MgMn_2O_4$ in magnesium batteries was first published independently by several research groups in 2015;[6] and thus, we explored both aqueous and non-aqueous electrolyte solutions, and both the electrochemical and chemical demagnesiation. After that, further papers have been published on the same electrode material,[4,7] and all these studies claim the potential application of $MgMn_2O_4$ in batteries. Nevertheless, this electrode material is not yet competitive compared to lithium batteries.

Potentially, the manganese spinel could operate in the region of Mn^{3+}/Mn^{4+} redox pair and in the region of Mn^{2+}/Mn^{3+} redox pair. Thus, one can find in the literature that some authors reported the electrochemical cycling experiments starting by discharge[7g,h] and others starting by charge.[7d,e] On the other hand, the stability of the spinel framework and the stability of the electrolyte solution in contact with the electrode material are very different depending on the voltage window. Shimokawa et al. reported that if one starts the electrochemical cycling by direct discharge, after Mg insertion into spinel oxides $A(II)B(III)_2O_4$ the B cations become divalent (Mn^{2+}), the cations located at the tetrahedral 8a sites (Mg(II)) are pushed out into

[a] A. Medina, A. I. Rodríguez, Prof. C. Pérez-Vicente, Prof. R. Alcántara
Department of Inorganic Chemistry
Instituto Universitario de Investigación en Química Fina y Nanoquímica (IUNAN)
University of Córdoba
Campus de Rabanales, Edificio Marie Curie
14071 Córdoba (Spain)
E-mail: ralcantara@uco.es

© 2021 The Authors. Chemistry - A European Journal published by Wiley-VCH GmbH. This is an open access article under the terms of the Creative Commons Attribution Non-Commercial NoDerivs License, which permits use and distribution in any medium, provided the original work is properly cited, the use is non-commercial and no modifications or adaptations are made.

Table 1. Calculated unit cell parameters for magnesiated and demagnesiated phases $Mg_xMn_{2-y}Fe_yO_4$ with normal spinel structure, corresponding to the reduction steps and volume variation represented in Figures 1 and 3, respectively.

	a–c [Å]	Vol. per formula [Å^3]	ΔVol. [%]
$Mg_2Fe_2O_4$	8.591	79.26	+2.89
$MgFe_2O_4$	8.510	77.03	0
Fe_2O_4	8.358	72.99	−5.24
$MgMn_{0.5}Fe_{1.5}O_4$	8.505	76.90	0
$Mg_{0.75}Mn_{0.5}Fe_{1.5}O_4$	8.443	75.22	−2.18
$Mn_{0.5}Fe_{1.5}O_4$	8.319	71.96	−6.42
MgMnFeO4	8.504	76.89	0
$Mg_{0.5}MnFeO_4$	8.348	72.71	−5.44
$MnFeO_4$	8.273	70.77	−7.96
$MgMn_{1.5}Fe_{0.5}O_4$	8.218–9.146	77.20	0
$Mg_{0.25}Mn_{1.5}Fe_{0.5}O_4$	8.266	70.60	−8.55
$Mn_{1.5}Fe_{0.5}O_4$	8.205	69.04	−10.57
$Mg_2Mn_2O_4$	8.706	82.48	+6.06
$MgMn_2O_4$	8.125–9.426	77.77	0
Mn_2O_4	8.158	67.86	−12.74

adjacent octahedral 16c vacant sites, the rocksalt phase A(II) $B(II)_2O_4$ is formed, and this phase transition from spinel to rocksalt could be reversible,[8] but the reversibility in prolonged charge/discharge cycling depends on the composition of the spinel. Gautam et al. found that the magnesium vacancies can facilitate the formation of Mg percolating networks by opening certain migration channels in the spinel $MgMn_2O_4$, while the inversion is a limiting factor of the electrochemical performance.[9]

One of the ways to improve the electrochemical behavior of the manganese oxide could be the partial demagnesiation previously to assembling the battery. The acid treatment of $LiMn_2O_4$ results in conversion to cubic λ-MnO_2, although some Li atoms remain in the oxide. The chemical and acid treatments of $MgMn_2O_4$ have been recently studied by several groups.[6a,c,7g] The cationic diffusion would be slower in $MgMn_2O_4$ compared to $LiMn_2O_4$. The particle size also influences on the kinetics of the acid treatment. The formation of Mg-vacancies could increase the mobility of magnesium and increase the faradic capacity. For example, if the starting composition is $Mg_{0.6}Mn_2O_4$, the theoretical capacity of the first discharge is 120 mAh g^{-1} before the transition to rocksalt structure. In addition, $MgMn_2O_4$ with tetragonal structure is transformed in a cubic structure after acid treatment, which is equivalent to the structure of λ-MnO_2. This is due to the disproportionation of Mn(III) into Mn(IV) and Mn(II) and the suppression of the tetragonal distortion induced by the Jahn-Teller effect of Mn(III).[6,10] Recent studies found a phase intermediate between $MgMn_2O_4$ and λ-MnO_2,[7f] although it could be affected by kinetics effects. We found that for partially demagnesiated $Mg_xMn_2O_4$, the Mn-vacancies can decrease the cell polarization.[7g] Other authors studied the relevant role of water content in the electrochemistry of $MgMn_2O_4$.[11]

The partial substitution of manganese by other elements such as iron has been proposed to suppress the oxidation of the electrolyte solution provoked by manganese ions.[7h,12] This manganese-substitution could improve the structure stability of the spinel, and it also could decrease the irreversible processes at the interface electrode/solution. On the other hand, the small particle size increases the electrochemical capacity because the short diffusion length compensates the slow diffusion rate of magnesium in the solids.

To achieve better electrochemical performance, it is necessary to further understand the mechanism of the intercalation/deintercalation, and to optimize the electrode composition. In this work we study the electrochemical (de)magnesiation and the acid-treatment of nanosized $MgMn_{2-y}Fe_yO_4$ samples for $0.4 \leq y \leq 2.0$. This is the first study about the acid treatment of the Mg–Fe-Mn spinels. Theoretical calculations are also employed.

Results and Discussion

Theoretical calculations

The theoretically calculated unit cell parameters (Table 1) of the compounds $MgFe_2O_4$, $MgMn_2O_4$ (both with spinel-type structure) and MnO_2 agree quite well with the experimental values (Table 2) and with those reported in the literature.[6,13] The theoretical calculations were also applied for compositions containing both iron and manganese by first time.

In the case of Mn-free $MgFe_2O_4$, the formation energy calculation indicates that the inverse spinel is ca. 50 meV per formula unit more stable than the normal spinel.[13] Besides the enthalpy, the entropy and synthesis conditions also could influence on the inversion as the actual degree of inversion depends on the temperature.[13] The calculated voltage for Mg extraction, involving the Fe^{3+} to Fe^{4+} oxidation, for both polytypes is very similar: 3.9 and 4.0 V vs. Mg for the normal and inverse spinel, respectively (Figure 1A), in agreement with

Table 2. Summary of the properties of $Mg_xMn_{2-y}Fe_yO_4$ samples.

	COMPOSITION			STRUCTURE	
	Nominal	XRF	Extrapolated	a, Å	L, nm
Raw samples	$MgMn_{1.6}Fe_{0.4}O_4$	$MgMn_{1.64}Fe_{0.39}$	$MgMn_{1.64}Fe_{0.39}O_4$	8.365(33)	8
	$MgMn_{1.2}Fe_{0.8}O_4$	$MgMn_{1.2}Fe_{0.76}$	$MgMn_{1.2}Fe_{0.76}O_4$	8.382(37)	9
	$MgMn_{0.4}Fe_{1.6}O_4$	$MgMn_{0.44}Fe_{1.56}$	$MgMn_{0.44}Fe_{1.56}O_4$	8.382(17)	14
	$MgFe_2O_4$	$MgFe_{2.0}$	$MgFe_2O_4$	8.381(32)	14
Acid-treated samples	$Mg_xMn_{1.6}Fe_{0.4}O_4$	$Mg_{0.77}Mn_{1.57}Fe_{0.43}$	$H_{0.06}Mg_{0.77}Mn_{1.57}Fe_{0.43}O_4$	8.380 (17)	6
	$Mg_xMn_{1.2}Fe_{0.8}O_4$	$Mg_{0.87}Mn_{1.18}Fe_{0.82}$	$H_{0.12}Mg_{0.87}Mn_{1.18}Fe_{0.82}O_4$	8.390 (12)	10
	$Mg_xMn_{0.4}Fe_{1.6}O_4$	$Mg_{0.79}Mn_{0.41}Fe_{1.59}$	$H_{0.24}Mg_{0.79}Mn_{0.41}Fe_{1.59}O_4$	8.382 (15)	15
	$Mg_xFe_2O_4$	$Mg_{0.85}Fe_{1.99}$	$H_{0.3}Mg_{0.85}Fe_{1.99}O_4$	8.383 (19)	16

© 2021 The Authors. Chemistry - A European Journal published by Wiley-VCH GmbH

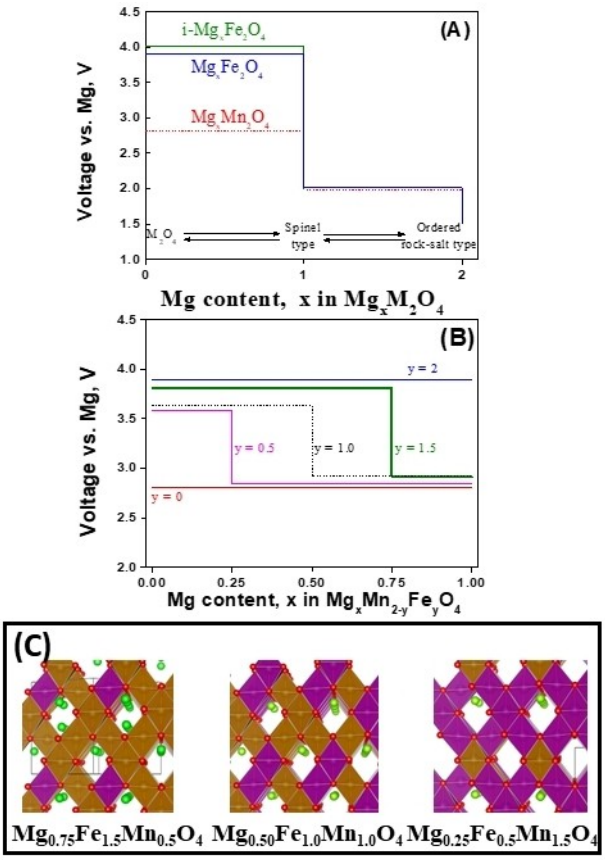

Figure 1. Calculated average voltage for the two main redox pairs Fe^{3+}/Fe^{4+} and Mn^{3+}/Mn^{4+} ($0 \leq Mg \leq 1$), and for the redox pairs Fe^{2+}/Fe^{3+} and Mn^{2+}/Mn^{3+} ($1 \leq Mg \leq 2$) for the following samples: (A) $MgMn_2O_4$ with normal spinel structure, and $MgFe_2O_4$, both with normal and inverse spinel structure, and (B) $MgFe_yMn_{2-y}O_4$ normal spinel structure. (C) Projection of the structure along the tunnels in the direction (1,1,0) of the spinel structure for the three intermediate stable phases, corresponding to the oxidation of Mn^{3+} to Mn^{4+} during demagnesiation. Color codes: in brown, Fe octahedra; in violet, Mn octahedra; and in green, Mg atoms.

previously published data for the normal spinel.[1c] However, the spinel inversion could hinder the electrochemical performance,[9] and thus it would not be desirable. The voltage of the Mg extraction using the redox pair Fe^{3+}/Fe^{4+} is ca. 1 V greater than that of the redox pair Mn^{3+}/Mn^{4+} (Figure 1B). These results would seem to indicate that the Fe-based system could be more interesting than the Mn-based system for the Mg extraction, because the energy density could be higher, but FeO_2 is not stable and decomposes into Fe_2O_3 and O_2. In addition, it could allow us to tailor the voltage of the battery by controlling the chemical composition of the spinel. However, it is expected that the hypothetic reversible oxidation Fe^{3+}/Fe^{4+} would be impossible and that the electrolyte solution would be oxidatively decomposed by Fe^{4+}. However, the redox pair Fe^{2+}/Fe^{3+} potentially could be used for reversible electrochemical cycling.

Three crystal structures obtained from DFT calculations are drawn in Figure 1C. Although the partially demagnesiated compositions (Fe-free) Mg_xMn_2O4 ($0.0 \leq x \leq 1.0$) are thermodynamically unstable,[6a,7g] the intermediate compositions of the $Mg_xMn_{2-y}Fe_yO_4$ series are found to be theoretically stable (Figure 2): $Mg_{0.25}Mn_{1.5}Fe_{0.5}O_4$, $Mg_{0.5}MnFeO_4$ and $Mg_{0.75}Mn_{0.5}Fe_{1.5}O_4$. Thus, according to the obtained Hull diagram, the spinels containing both Fe and Mn could be more stable and would allow to achieve further electrochemical cycling.

The calculated volume change during Mg deintercalation is represented in Figure 3. For $MgFe_2O_4$, the volume contraction is only 5.2%, in agreement with the smaller size of Fe^{4+} (0.585 Å) as compared to Fe^{3+} (0.645 Å). These compounds have no Jahn-Teller distortion, and the volume variation in the Fe-based system is considerably smaller than that of the Mn-based system. For $MgMn_2O_4$, the volume reduction is more important (ca. 13%). This is due to the additional expansion in the pristine material due to the cooperative Jahn-Teller distortion induced by Mn^{3+} cations. After Mg deintercalation from $MgMn_2O_4$, Mn^{3+} (0.645 Å) is oxidized to Mn^{4+} (0.53 Å), the cell is contracted and and the Jahn-Teller distortion disappears.

For the intercalation of more than one Mg per formula unit ($x > 1$ in $Mg_xMn_{2-y}Fe_yO_4$), the reduction from the trivalent to the divalent oxidation state would take place at ca. 2.0 V for both iron and manganese, and the formation of the rocksalt structure is expected (Figure 1A). The change of the voltage during the charge/discharge process would be greater for compositions

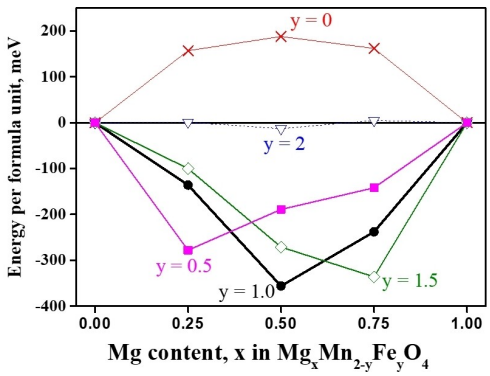

Figure 2. Hull diagram.

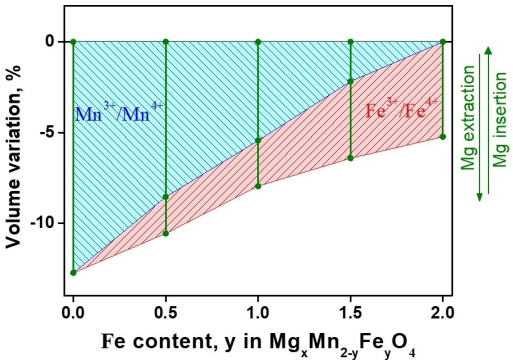

Figure 3. Calculated relative volume variation for $Mg_xMn_{2-y}Fe_yO_4$ during Mg deintercalation. The variations assigned to Fe^{3+}/Fe^{4+} and Mn^{3+}/Mn^{4+} redox pairs are indicated.

© 2021 The Authors. Chemistry - A European Journal published by Wiley-VCH GmbH

with higher iron content, particularly when the magnesium-content moves between $x<1$ and $x>1$, and it can involve changing the oxidation states of the transition elements between +2 and +4.

XRD and TEM

The structures of the prepared samples $MgMn_{2-y}Fe_yO_4$ samples were studied by using XRD. The XRD patterns (Figure 4) of all the samples agree well with spinel-type structure. The broad reflections indicate small particle size. As due to the small particle size and large broadening of the reflections, a proper refinement of the structure using the method of Rietveld is not possible, and the inversion cannot be properly elucidated. It is expected that the inversion degree increases with the iron content, from the ideal normal spinel $[Mg^{2+}]_T[Mn^{3+},Mn^{3+}]_OO_4$ to the ideal inverse spinel $[Fe^{3+}]_T[Mg^{2+},Fe^{3+}]_OO_4$, because of the preferential occupancy of octahedral coordination by Mn^{3+}. In that sense, the change of the relative intensity of the (111) reflection strongly suggests that the distribution of the ions is modified. All the resulting XRD patterns are ascribed to the cubic phase and the space group Fd3m (Figure 4A). The unit cell parameters of the phases were calculated using the full pattern matching method, and these are given in Table 2, together with the average crystallite size (L). The replacement of Mn^{3+} (Jahn-Teller ion) by Fe^{3+} (no Jahn-Teller ion), can contribute to stabilize the cubic spinel, compared to tetragonal $MgMn_2O_4$. The lattice cell parameter is very similar for all the samples, because the radii of Mn^{3+} and Fe^{3+} are equivalent (0.645 Å). There is a certain tendency to increase the crystallinity and the crystallite size with the iron content.

Through simulations of the XRD patterns with different cationic distributions (Figure 4C), it is obtained that the significant difference between them is that the increasing of the inversion degree involves decreasing the relative intensity of the (111) reflection. Thus, it is experimentally observed in Figure 4A that for higher iron-content the intensity of the reflection (111) at ca. 18° 2θ decreases, confirming that the samples with more iron are more reversed. According to Gautam et al., this structural disorder can limit the electrochemical capacity.[9]

The XRD patterns and the resulting structure for the samples after acid treatment are shown in Figure 4B and Table 2, respectively. The acid-treatment to remove magnesium ions from the structure of the spinel has little influence on the unit cell parameter of the cubic cell, as expected, because magnesium is a small ion. The samples with higher Fe-content still have narrower reflections and larger crystallite size. Interestingly, the samples with lower Mn-content still exhibits higher relative intensity of the (111) reflections

The particle morphology was examined by TEM (Figure 5). All the samples are powders composed by nanometric particles with irregular morphology. The diameter of the particles is around 10–50 nm. For the raw samples (Figure 5a and b) it is observed that the particle size tends to increase with the iron

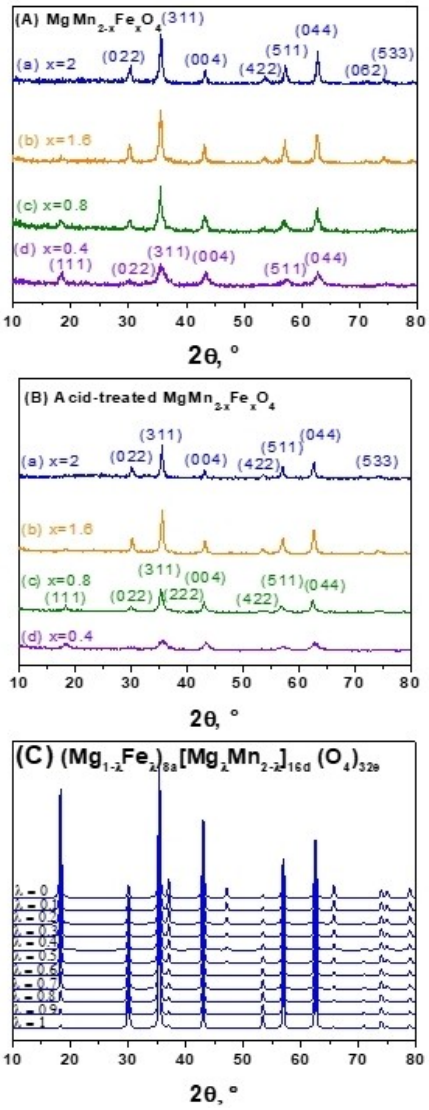

Figure 4. XRD patterns of $MgMn_{2-y}Fe_yO_4$ samples before (A) and after (B) acid-treatment. The Miller indexes of the main reflections are indicated. (C) Calculated XRD patterns with different inversion degrees.

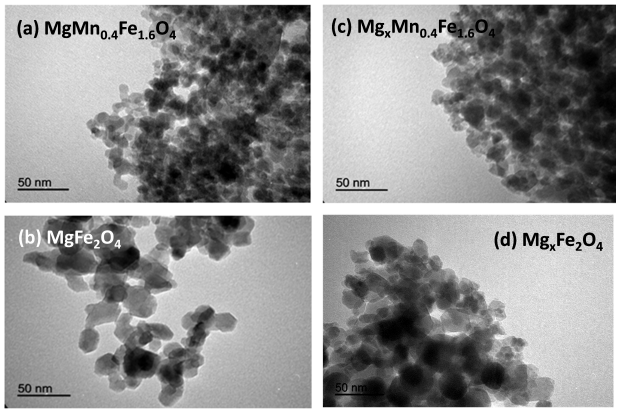

Figure 5. Selected TEM micrographs of samples before (a, b) and after (c, d) acid treatment.

© 2021 The Authors. Chemistry - A European Journal published by Wiley-VCH GmbH

content. Significant change of the particle size and morphology is not observed after acid-treatment (Figure 5 c and d). Using microanalysis coupled to SEM and elements mapping (not shown), it was checked that the distribution of the elements in the nanoparticles was homogeneous before and after acid treatment.

Acid treatment

The relative amounts of the metallic elements (Mg, Mn, and Fe) in all the prepared samples were analyzed by using XRF (Table 2). For the raw samples, the experimental compositions agree well with the expected results, or nominal compositions, and we can assume the stoichiometry $MgMn_{2-y}Fe_yO_4$. After the treatment with acid solution, the experimental Mg-content decreases for all the samples, as expected. The deinsertion of magnesium is substantially lower for Fe-containing spinels compared to the results previously reported for Fe-free $MgMn_2O_4$. This result agrees well with the Hunter's mechanism based on the Mn^{3+} disproportionation as the main mechanism for demagnesiation in the acid solution.[14] Nevertheless, a small amount of Mg is extracted even from Mn-free $MgFe_2O_4$. It is known that Mn(III) is not stable against disproportionation reaction, while Fe(III) and Fe(II) are stable. Consequently, the disproportionation of manganese cannot be the only mechanism involved in the acid-treatment. Knight et al. found that Zn is not extracted from $ZnMnNiO_4$, because this compound does not contain Mn^{3+}, and the disproportionation would be the only possible mechanism for Zn extraction from this spinel.[10] Our results can be related with the higher disorder and inversion degree in the iron-containing spinels, because protons can be exchanged with the cations in the octahedral sites of the inverse spinel (Mg^{2+} in $MgFe_2O_4$), but protons do not exchange with the cations in the tetrahedral site of normal spinel (Zn^{2+} in $ZnMnNiO_4$ and Mg^{2+} in ideal $MgMn_2O_4$).[10] Analogously, Knight et al. found that the increasing of the cation order increases the rate of Mg removal from $MgMn_2O_4$.[6c]

For $MgMn_2O_4$, the disproportionation of Mn(III) is the mechanism in the acid-treatment, only the Mg extraction reaction takes place and the magnesium/proton exchange is negligible, as it was previously reported.[6] Thus, this process is summarized in the next reaction:

$$(1+x)MgMn_2O_4(s) + (8x)H^+(aq.) \rightarrow Mg_{1-x}Mn_2O_4(s) + (2x)Mn^{2+}(aq.) + (2x)Mg^{2+}(aq.) + (4x)H_2O(l) \quad (1)$$

The mechanism of the disproportionation reaction (1) involves that two Mn^{3+} ions being next to each other are converted into one Mn^{4+} and one Mn^{2+}. It is known that the degree of inversion can affect to the disproportionation reaction, because for each Mg^{2+} in an octahedral site, a Mn^{2+}–Mn^{4+} pair is formed instead of two Mn^{3+}, and this also induces a decrease of the tetragonal distortion.[15] Consequently, the presence of Fe^{3+} ions would decrease the formation of neighboring Mn^{3+}–Mn^{3+} that can disproportionate, similarly to mechanism proposed for Al^{3+}-doped spinel.[6c] However, we could not completely discard that the redox pair Fe^{3+}/Fe^{2+} could help to the electron jump from one Mn to another Mn.

The experimental x-value in $Mg_{1-x}Mn_{2-y}Fe_yO_4$ after the acid-treatment is between $x=0.13$ and $x=0.23$. The experimental atomic ratio Mn/Fe slightly decreases after acid treatment (Table 2), indicating that a small amount of Mn is dissolved and, consequently, manganese vacancies are created. For Mn-free sample $MgFe_2O_4$ the smaller amount of magnesium which is deinserted cannot be ascribed to the disproportionation reaction (1), iron dissolution from the lattice is not expected, and the chemical exchange between magnesium and protons must be the mechanism of the acid-treatment reaction:

$$MgFe_2O_4(s) + (2x)H^+(aq.) \rightarrow H_{2x}Mg_{1-x}Fe_2O_4(s) + xMg^{2+}(aq.) \quad (2)$$

According to the experimental compositions and the literature about $MgMn_2O_4$, one could conclude that the reaction (2) is slower than the reaction (1), but the particle size and the structural disorder also could influence on the kinetics of the processes. It is expected that the cationic disorder in the spinel structure favors the exchange mechanism against the disproportionation reaction. In fact, the two reactions given above can contribute to the chemical demagnesiation for the compounds containing both Fe and Mn, and the relative contribution of the exchange reaction would increase compared to the disproportionation reaction when the Fe-content increases.

For the acid-treated samples, the approximate hydrogen content was extrapolated according to reaction (2). Thus, using the general formula $H_{2x}Mg_{1-x}Mn_{2-y}Fe_yO_4$, if one accepts that for the sample with $y=2$ there is only cation exchange, and the relative amounts of magnesium and iron are experimentally measured, then we assume the formula of the chemically demagnesiated Mn-free sample must be $H_{0.3}Mg_{0.85}Fe_{1.99}O_4$. After considering that for $x=0$ only chemical disproportionation occurs (no chemical exchange), and that the proton-content is related to the iron content analogously to $H_{0.3}Mg_{0.85}Fe_{1.99}O_4$, then we assume the stoichiometry-derived linear relationship $2x=0.15y$, and finally one can extrapolate the expected maximum H-content for the samples containing both Fe and Mn. The chemical compositions which are extrapolated using this procedure are shown in Table 2.

On the other hand, the chemical exchange magnesium/proton does not involve the dissolution of any manganese, in contrast to the disproportionation reaction. More cationic vacancies are created when the iron-content is smaller.

We cannot discard that the chemical reactions written above to discuss the acid-treatment which involve protons, water, and metal ions, also affect to the electrochemical behavior. The traces of water in the electrolyte solution or in the electrode materials could induce chemical reactions in the electrochemical cell, in addition to the main electrochemical reaction, and it could affect to the electrochemical cycling. Thus, traces of water in the electrolyte could induce chemical

© 2021 The Authors. Chemistry - A European Journal published by Wiley-VCH GmbH

exchange proton-magnesium and/or disproportionation, similarly to the acid treatment that we have studied above, and it should be further studied in future works.

The thermal behavior of the acid-treated powders was studied by TGA (Figure 6). For the composition $H_{0.3}Mg_{0.85}Fe_{1.99}O_4$, the theoretical mass loss would be between 0.15% (for protons in the form of H^+) and 2.8% (for protons in the form of H_3O^+). From the TGA of all the acid-treated samples, it is found that the mass loss up to 550 °C is within the range between 8.3% and 1.3%. On the other hand, it is worth to note that the acid treatment of the manganese oxides nanoparticles can lead to surface protonation and adsorption of water. Thus, in the seminal paper of Thackeray et al. about extraction of Li from $LiMn_2O_4$ and the disproportionation reaction of manganese the authors wrote that the adjustment to an oxygen deficiency at the surface of an oxide particle in an aqueous medium is made by binding water.[14b] The water content of our samples is affected by the different ways throughout the samples can get water, not only the exchange reaction between magnesium and proton.

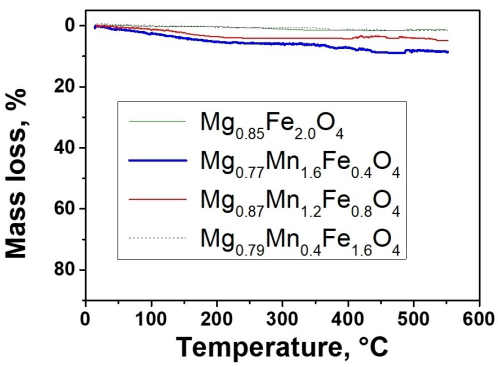

Figure 6. TGA curves for the acid-treated spinels.

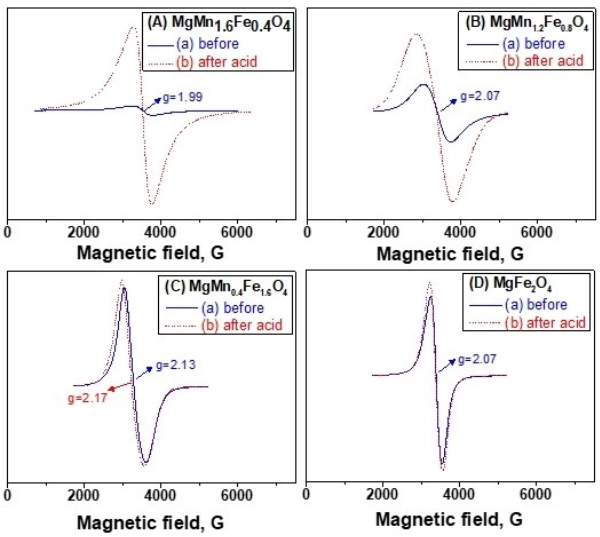

Figure 7. ESR spectra of $MgMn_{2-y}Fe_yO4$ samples before and after acid treatment.

ESR

The ESR spectroscopy is very sensitive to the oxidation states of the paramagnetic ions and the interactions between them.[16] The ESR signals at room temperature of selected spinel samples are shown in Figure 7. According to the literature, it is expected that Fe^{3+} ions (^6S) in octahedral B site of the spinel give a broad signal centered at $g \approx 2.0$,[13a,16] and our results for $MgMn_{2-y}Fe_yO_4$ agree well with the presence of iron in octahedral site. On the other hand, one could believe that Mn(III) is ESR-silent, but it has been reported that Mn(III) can contribute to the ESR line when it is in a strongly Jahn-Teller distorted octahedral site and Mn(IV) impurities also could contribute to the signal.[15,16] All these Fe-containing samples exhibit relatively narrow ESR signals, compared to iron-free sample,[7g] because of the superexchange interactions. For the compound $MgMn_{1.6}Fe_{0.4}O_4$ the broadening of the ESR line (Figure 7Aa) is $\Delta H \approx 515$ G, and after acid treatment (Figure 7Ab) the line becomes more intense and isotropic, and it is still centered at $g = 1.99$. It is evident that, after acid treatment, the disproportionation of Mn(III) into Mn(II) and Mn(IV) increases the intensity of the signal. For higher iron contents the signals become more broadened: $\Delta H \approx 702$ in Figure 6Ba, and $\Delta H \approx 560$ G in Figure 7Ca. For even higher iron-content (Figure 7Ca and Da), the spectra centered at $g \approx 2.1$ are equivalent to the spectrum previously reported for $MgFe_2O_4$,[13a,16b] which is due to Fe^{3+} ions in octahedral site. The narrower signal ($\Delta H \approx 311$ G) is observed for (Mn-free) $MgFe_2O_4$ (Figure 7Da). Most probably, the increasing of the degree of inversion concomitant to the increasing of the iron content yields to stronger $[Fe^{3+}]_A$–O–$[Fe^{3+}]_B$ superexchange interactions and narrower ESR line. After acid treatment, the spectra remain almost unchanged in Figures 7Cb and 7Db, in good agreement with the exchange magnesium/proton reaction while the transition metal ions remain nearly unchanged. There is a very slight increase of the linewidth that can be due to stronger magnetic dipolar interactions and weaker susperexchange interactions because of proton incorporation Thus, proton intercalation can weaken the superexchange interactions and broaden the ESR line. The observed tendency is that the spectra are more strongly changed after acid-treatment for the samples with lower iron-content (Figure 7Ab and 7Bb). As a conclusion, the ESR spectra agree well with the different mechanisms that we have proposed for the acid treatment depending on the Mn/Fe relative content: disproportionation for manganese, cationic exchange and no change of oxidation state for iron, and a mixture of the two mechanisms for the intermediate compositions containing both Fe and Mn atoms.

Electrochemistry

There are several reasons to think that the electrochemical behavior could be improved for the Fe-containing spinels: the theoretically calculated change of the unit cell volume during the intercalation/deintercalation of magnesium is smaller (Table 1), the distortion of the unit cell due to the Jahn-Teller effect in Mn^{3+} is not expected, the intermediate composition

© 2021 The Authors. Chemistry - A European Journal published by Wiley-VCH GmbH

can be thermodynamically more stable, and the lower Mn^{3+}-content can help to avoid the electrolyte decomposition. On the other hand, the cations vacancies created after acid treatment and the small particle size could improve the diffusion of magnesium and allow rapid charge-discharge, although this effect would be more limited for Fe-containing spinels compared to Fe-free $MgMn_2O_4$. Thus, despite the difficulties inherent to magnesium batteries, it is worthy to explore the electrochemical behavior of the prepared samples in magnesium cells.

The electrochemical behavior of all the prepared samples was studied, but only the most significant ones are shown, particularly because a high inversion degree of the spinel with high-iron content can limit the electrochemical response. The selected results of the electrochemical experiments in three-electrode cells are shown in Figure 8. For comparison, the voltage curve of the working electrode (spinel) is measured against Mg (reference electrode) and activated carbon (counter electrode). The electrolyte solutions and the lack of an ideal reference electrode can influence on the deviations of the experimental voltage compared to the DFT calculations. The electrochemical cycling for the reversible electrochemical activity of iron would be limited to Fe^{2+}/Fe^{3+} because the hypothetical oxidation to Fe^{4+} at high voltage would oxidize the electrolyte. In contrast to iron, the reversible redox activity of manganese could involve the two redox pairs Mn^{2+}/Mn^{3+} and Mn^{3+}/Mn^{4+}. If one starts the electrochemical cycling by discharging firstly, the transition elements would be reduced from Mn^{3+} to Mn^{2+} and from Fe^{3+} to Fe^{2+}, and then the charge capacity could be higher than the previous discharge capacity only if manganese ions be oxidized to Mn^{4+}. The first discharge is different from the subsequent ones, and the (partial) transition from spinel-type to ordered rocksalt structure during the first discharge could be a reason for that. A dynamic change of the spinel inversion during discharge/charge also can contribute to the polarization and voltage hysteresis.[9] According to the voltage-capacity curves, the reoxidation from divalent to trivalent stat of the transition elements happens through a sloped voltage region below ca. 2.4 V vs. Mg., and the oxidation up to Mn^{4+} occurs at a pseudoplateau at ca. 2.5 V vs. Mg (or

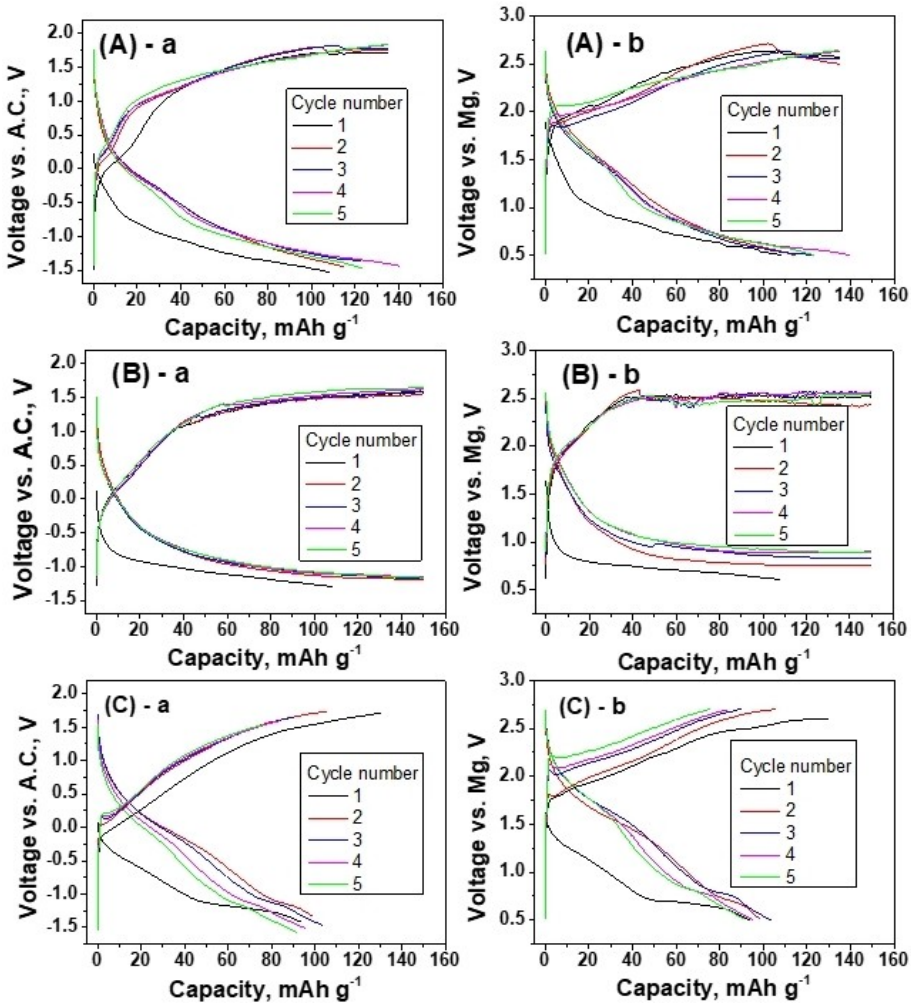

Figure 8. Voltage-capacity curves for the selected working electrodes: (A) $MgMn_{1.6}Fe_{0.4}O_4$, (B) $MgMn_{1.2}Fe_{0.8}O_4$ and (C) acid-treated $MgMn_{1.6}Fe_{0.4}O_4$. The plotted voltage was measured against: (a) activated carbon counter electrode and (b) Mg reference electrode. The electrochemical cycling was started firstly by discharging.

© 2021 The Authors. Chemistry - A European Journal published by Wiley-VCH GmbH

1.5 V vs. activated carbon). This pseudoplateu at ca. 2.5 V is only ca. 0.6 V lower than the theoretically calculated value. Han et al. pointed out that the iron cations are less electrochemically active than the manganese ones towards catalyzing the electrolyte oxidation.[7h]

For $MgMn_{1.6}Fe_{0.4}O_4$, the reversible capacity is around 110–140 mAh g^{-1} (Figure 8A). For $MgMn_{1.2}Fe_{0.8}O_4$ (Figure 8B), it is observed that the initial voltage drop in the first discharge is more rapid, also the voltage rise in the charge is more abrupt and, consequently, the (de)intercalation of magnesium is more difficult for this composition. Most probably, the disorder in the Fe–Mn spinel makes that the diffusion of magnesium in the host be more difficult, in good agreement with the XRD results shown above and which indicate that the cationic distribution in tetrahedral/octahedral sites change with the iron content. In conclusion, the reversible redox activity is mainly due to Mn^{2+}/Mn^{3+}, and the simultaneous presence of manganese and iron could be beneficious for protecting again electrolyte decomposition, like it was proposed by Han et al. for experiments carried out at 100 °C.[7h] However, the relative amount of iron should be limited, and we think that this effect is analogous to the known effect of Al-doping in some layered-type cathodes for lithium-ion batteries. The influence of the spinel inversion, due to iron in tetrahedral sites, on the electrochemistry should be further examined in future works.

For the acid-treated sample, since the Mg-content is lower than one Mg per formula, the formation of the rocksalt-type structure after the first discharge would be reduced. This effect results in different voltage curves for the first discharge in Figure 8Ab and 8Cb. This fact would be beneficious for the kinetics of charge/discharge. In contrast to previous results about acid-treated (Fe-free) $MgMn_2O_4$, the acid-treatment does not reduce the voltage polarization for Fe-containing spinels (Figure 8C) after the first discharge, and the reason is that the mechanisms of the acid-treatment are different and the creation of cationic vacancies is less significant for Fe-containing spinels, as it was discussed above. In the voltage-magnesium content for $Mg_xMn_{1.6}Fe_{0.4}O_4$ curve (Figure 9), it is observed that the during the second discharge the initial amount of Mg in the acid-treated sample is recuperated at

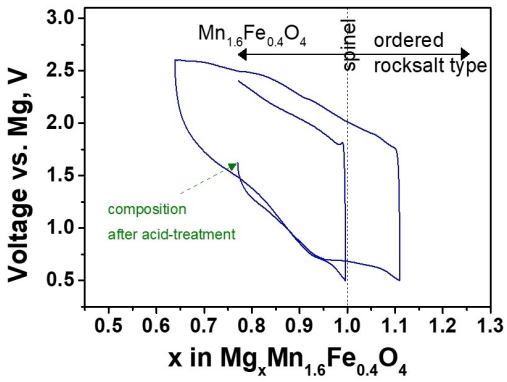

Figure 9. Voltage measured against Mg and plotted vs. Mg-content for acid-treated $MgMn_{1.6}Fe_{0.4}O_4$.

nearly the same voltage (around 1.5–1.6 V vs. Mg). The results agree well with the reversibility of the (de)magnesiation, in the different regions for $x > 1.0$ and $x < 1.0$.

The cyclic voltammogram (CV) was investigated using three-electrode cell (Figure 10A–E) with A.C. as counter electrode and Mg as reference electrode. The CV was started by reductive scan from OCV to 0.5 V at 20 mv s^{-1} of scan rate, stopped at the end of the oxidative sweep, and then restarted at a different rate. The oxidative decomposition of the electrolyte solution starts at ca. 2.7 V and, thus, the reversible oxidation of the transition metals to the tetravalent state would not be very efficient under these experimental conditions. The presence of cathodic and anodic peaks at slow scan rate and below 2.6 V is in good agreement with the reversible intercalation of magnesium in the spinel framework, and the reversible change of the trivalent/divalent oxidation state. The observed evolution of the CV with the scan rate suggests that the diffusion of magnesium in the spinel is relatively sluggish. To further understand the origin of the electrochemical capacity, the CV recorded at several rates can be used. According to the literature and the relationship $i = a\ v^b$, the b-value can be obtained from the plot of log i versus log v, where i is the current and v is the scan rate (Figure 10F).[17] For the ideal diffusion-controlled faradaic process $b = 0.5$. If $b = 1.0$, the process is a surface reaction involving a non-diffusion-controlled process (or capacitive). For the reduction peak observed near 1.5 V (Figure 10), the resulting value is $b = 0.69$. Consequently, the electrochemical reaction is mainly controlled by a diffusion process, as expected for magnesium intercalation. The current of the reduction peak near 1.5 V arises from magnesium insertion into the spinel, although a small capacitive contribution cannot be discarded.

To remove any interference of the Mg electrode in the electrochemical cycling, for the selected sample acid-treated $MgMn_{1.6}Fe_{0.4}O_4$, the electrochemical behavior in two-electrode cell with activated carbon as counter electrode is shown in Figure 11. In this case, the cycling started in charge mode (oxidation at the working electrode) and the formation of ordered salt-rock is avoided. The maximum discharge capacity is around 120–127 mAh g^{-1}, which is equivalent to the range of composition $0.6 < x < 1.0$ in $Mg_xMn_{1.6}Fe_{0.4}O_4$. The charge capacity over ca. 1.6 V vs. activated carbon is irreversible, particularly at low rate (5 mA g^{-1} of current density), very probably due to the oxidative decomposition of the electrolyte solution catalyzed by the transition elements. The electrostatic repulsion between magnesium and oxidized manganese could slow down the mobility of magnesium and reduce the charge capacity. The discharge capacity is lower at higher current density (Figure 11B), indicating that the diffusion of magnesium is not very rapid. Probably, with another electrolyte solution the reversible capacity could be higher.

Conclusion

The DFT calculations unveil that the intermediate compositions of the spinels containing both Fe and Mn could be more stable

© 2021 The Authors. Chemistry - A European Journal published by Wiley-VCH GmbH

than the extreme compositions, and that the Fe/Mn composition can tailor the voltage of the oxidation and demagnesiation; and it is worthy to explore them. Nanoparticles of magnesium-manganese-iron oxide samples were successfully prepared following a modification of Pechini method. The iron-containing samples exhibit XRD patterns corresponding to cubic spinel. The extraction of magnesium from $MgMn_{2-y}Fe_yO_4$ has been explored by acid-treatment, and it is experimentally found that after this acid-treatment, the relative amount of magnesium decreases. The effect of the acid-treatment in $MgMn_{2-y}Fe_yO_4$ is different for Fe-containing spinels compared to iron-free $MgMn_2O_4$; and two different reactions have been proposed: disproportionation of Mn(III) and magnesium deintercalation, and exchange between Mg in tetrahedral sites and protons. The reversible charge/discharge process can involve the change of the oxidation states from Mn^{2+} to Mn^{4+} and from Fe^{2+} to Fe^{3+}. Thus, the replacement of manganese by iron limits the capacity and can improve the cycling stability. The maximum reversible capacity is 120 mAh g^{-1}, which below the theoretical maximum capacity, and then we think that it would be worthy to explore the electrochemical cycling of these materials with other electrolyte solutions in future works.

Experimental Section

Synthesis: The preparation of the powdered samples with general composition $MgMn_{2-y}Fe_yO_4$ ($0.4 \leq y \leq 2.0$) was based in a modification of Pechini's method.[6a] This method of synthesis was chosen to obtain small particle size and to reduce the diffusion path length. Firstly, stoichiometric amounts of $Mg(NO_3)_2 \cdot 6H_2O$, $Mn(NO_3)_2 \cdot 4H_2O$ and $Fe(NO_3)_3 \cdot 9H_2O$ were dissolved in a beaker with water. Secondly, citric acid and ethyleneglycol were added to the solution with a molar ratio metals: citric acid : ethylene glycol = 1.5:3.0:9.0. After heating to 70 °C with continue stirring, the resulting slurry was calcinated at 200 °C. The obtained product was grinded and finally annealed at 400 °C during 10 h.

The partial demagnesiation of $MgMn_{2-y}Fe_yO_4$ nanoparticles was performed by using acid-treatment.[6a,7g,14] The raw sample was added to a solution of nitric acid at pH = 2 with continue stirring for two hours. The resulting solid product was separated by ultra-centrifugation, washed with distilled water, and dried at 90 °C under vacuum.

Microstructure and composition: The crystalline phases were characterized by X-ray diffraction (XRD). The XRD patterns were recorded using Bruker D8 Discover A25 equipment provided with CuKα radiation, Ge monochromator and Lynxeye detector. The XRD patterns were fitted and the lattice cell parameters were calculated using the full pattern matching method, as implemented in the commercial software Topas 4.2. The microstructure of the particles

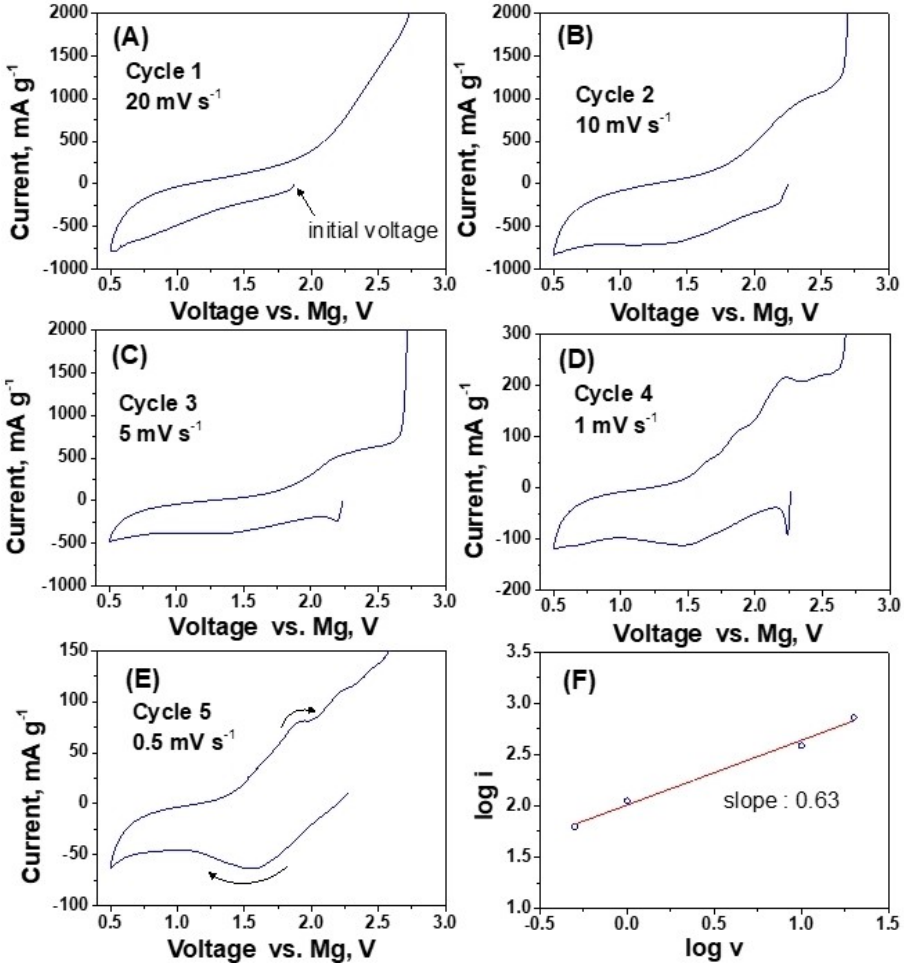

Figure 10. (A–E) CV obtained at different rates, and (F) plot of *log i* vs. *log v*, for acid-treated $MgMn_{1.6}Fe_{0.4}O_4$.

© 2021 The Authors. Chemistry - A European Journal published by Wiley-VCH GmbH

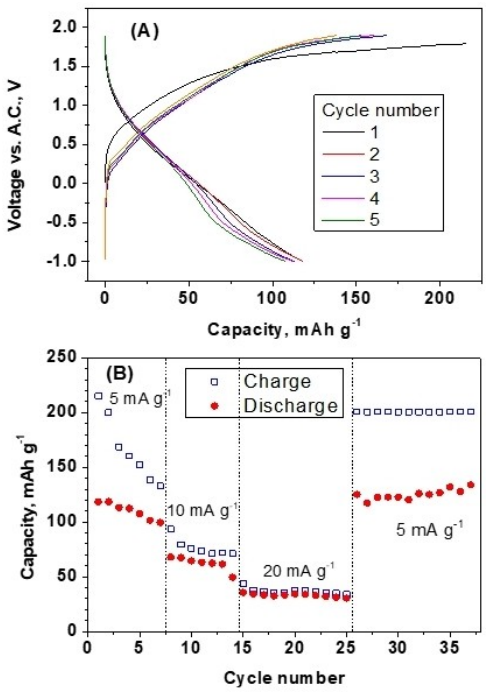

Figure 11. Electrochemical results of acid-treated $MgMn_{1.6}Fe_{0.4}O_4$ in two-electrode cell and starting the cycling by firstly charging. (A) Voltage-capacity curves. (B) Specific capacity value as a function of cycle number under variable current intensity.

was studied by Transmission Electron Microscopy (TEM) using a JEM-1400 instrument. To determine the chemical compositions (Mg, Mn, and Fe) of the samples, the spectrometer Rigaku Primus IV of X-Ray Fluorescence (XRF) was employed. Thermogravimetric Analysis (TGA) was carried out in a Shimadzu instrument, under static air atmosphere at 5 °C min.$^{-1}$ of heating rate. Electron Spin Resonance (ESR) spectra were recorded in a Bruker EMX instrument, operating at X-band and 9.75 GHz.

Electrochemistry. A VMP instrument and three-electrode cells were employed to carry out the electrochemical experiments. The Swagelok-type cells with T-shape were assembled in an Ar-filled glovebox equipped with sensors of oxygen and water. A piece of Mg (Panreac) was used as a reference electrode and activated carbon as a counter electrode. The working electrodes were formed by active material (80 %), binder (PVDF, 10 %) and carbon black (10 %) pressed on a Ti (Goodfellow) current collector. The electrolyte solution was 1 M anhydrous $MgClO_4$ (Sigma-Aldrich) in dry acetonitrile (ACN) (Sigma-Aldrich), impregnated in Whatman glass fiber papers.

Calculations. The structure calculations were performed within the density functional theory (DFT), as implemented in the CASTEP code.[18] We use the Generalized-Gradient Approximation (GGA) with the PBEsol correlation potential, and "on-the-fly" generated pseudopotentials of CASTEP code. The internal coordinates were optimized using the BFGS algorithm, while the energy minimization was carried out using a density-mixing scheme with a conjugate-gradient Pulay solver. The cut-off energy was fix at 550 eV. Spin polarized calculations were performed in all cases. The selected k-point mesh was of ca. 0.07 Å^{-1}, according to the Monkhorts-Pack scheme. The convergence conditions were: energy, 10^{-5} eV per atom; max. force, 0.03 eV Å^{-1}; max. stress 0.05 GPa, max. displacement, 10^{-3} Å. For the GGA + U correction we used the value U_{eff} = 3.9 for Mn, and 5.3 eV for Fe.[1c] In all the calculations we assumed that the host spinel framework M_2O_4 remains basically unchanged during the Mg de-insertion and reinsertion processes, excepting the tetragonal distortion induced by Mn (III) cations. Unit cell parameters and atomic coordinated were relaxed. The different structures $Mg_xMn_{2-y}Fe_yO_4$ were defined as follow: for y = 0 the classical tetragonal spinel structure was used as starting point; for y = 0.5 and y = 1.5 a cation distribution of Fe and Mn similar to that found in $LiNi_{0.5}Mn_{1.5}O_4$ was assumed;[19] for y = 1 the cation distribution was the same used for $MgNiMnO_4$;[20] and for deficient Mg samples, as already described for $MgMn_2O_4$.[7g]

Acknowledgements

This work was supported by MINECO (grant number MAT2017–84002-C2–1-R), and Junta de Andalucía (research group FQM288). We express thanks to SCAI-UCO (TEM) and the IUNAN (ESR, XRD and XRF) for facilitating scientific instruments.

Conflict of Interest

The authors declare no conflict of interest.

Keywords: computational chemistry · intercalation · magnesium batteries · spinel · X-ray diffraction

[1] a) Y. Liang, H. Dong, D. Aurbach, Y. Yao, *Nat Energy* **2020**, *5*, 646–656; b) D. Li, Y. Yuan, L. Liu, M. Fichtner, F. Pan, *J. Magnes. Alloy.* **2020**, *8*, 963–979; c) M. Liu, Z. Rong, R. Malik, P. Canepa, A. Jain, G. Ceder, K. A. Persson, *Energy Environ. Sci.* **2015**, *8*, 964–974; d) M. Cabello, A. Medina, R. Alcántara, F. Nacimiento, C. Pérez-Vicente, J. L. Tirado, *J. Alloys Compd.* **2020**, *831*, 154795–154808; e) S. Tan, F. Xiong, J. Wang, Q. An, L. Mai, *Materials Horizon* **2020**, *7*, 1971–1995; f) C. Pei, F. Xiong, Y. Yin, Z. Liu, H. Tang, R. Sun, Q. An, L. Mai, *Small* **2021**, *17*, 2004108–2004138.

[2] a) P. Canepa, G. Sai Gautam, D. C. Hannah, R. Malik, M. Liu, K. G. Gallagher, K. A. Persson, G. Ceder, *Chem. Rev.* **2017**, *117*, 4287–4341; b) H. Li, W. Zhang, K. Sun, J. Guo, K. Yuan, J. Fu, T. Zhang, X. Zhang, H. Long, Z. Zhang, Y. Lai, H. Sun, *Adv. Energy Mater.* **2021**, 2100867–2100902.

[3] a) R. Mohtadi, F. Mizuno, *Beilstein J. Nanotechnol.* **2014**, *5*, 1291–1311; b) S. Y. Ha, Y. W. Lee, S. W. Woo, B. Koo, J. S. Kim, J. Xho, K. T. Lee, N. S. Choi, *ACS Appl. Mater. Interfaces* **2014**, *6*, 4063–4073.

[4] R. D. Bayliss, B. Kay, G. S. Gautam, P. Canepa, B. J. Kwon, S. H. Lapidis, F. Dogan, A. A. Adil, A. S. Lipton, P. J. Baker, G. Ceder, J. T. Vaughey, J. Cabana, *Chem. Mater.* **2020**, *32*, 663–670.

[5] a) T. Ichitsubo, T. Adachi, S. Yagi, T. Doi, *J. Mater. Chem.* **2011**, *21*, 11764–11772; b) J. N. Cha, B. S. Cheong, H. G. Cho, *J. Phys. Chem. A* **2001**, *105*, 1789–1796; c) M. Salama, I. Shterenberg, L. J. W. Shimon, K. Keinan-Adamsky, M. Afri, Y. Gofer, D. Aurbach, *J. Phys. Chem. C* **2017**, *121*, 24909–24918.

[6] a) M. Cabello, R. Alcántara, F. Nacimiento, G. Ortiz, P. Lavela, J. L. Tirado, *CrystEngComm* **2015**, *17*, 8728–8735; b) S. Okamoto, T. Ichitsubo, T. Kawaguchi, Y. Kumagai, F. Oba, S. Yagi, K. Shimokawa, N. Goto, T. Doi, E. Matsubara, *Adv. Sci.* **2015**, *2*, 1500072–1500081; c) J. C. Knight, S. Therese, A. Manthiram, *ACS Appl. Mater. Interfaces* **2015**, *7*, 22953–22961.

[7] a) V. Soundharrajan, B. Sambandam, S. Kim, V. Mathew, J. Jo, S. Kim, J. Lee, S. Islam, K. Kim, Y. K. Sun, J. Kim, *ACS Energy Lett.* **2018**, *3*, 1998–2004, b) S. Tao, W. Huang, Y. Liu, S. Chen, B. Qian, L. Song, *J. Mater. Chem. A* **2018**, *6*, 8210–8214; c) Q. D. Truong, M. K. Devaraju, P. D. Tran, Y. Gambe, K. Nayuki, Y. Sasaki, I. Honma, *Chem. Mater.* **2017**, *29*, 6245–6251; d) Q. D. Truong, H. Kobayashi, K. Nayuki, Y. Sasaki, I. Honma, *Solid State Ion.* **2020**, *344*, 115136–115142; e) T. Hatakeyama, N. L. Okamoto, K. Shimokawa, H. Li, A. Nakao, Y. Uchimoto, H. Tanimura, T. Kamaguchi,

© 2021 The Authors. Chemistry - A European Journal published by Wiley-VCH GmbH

T. Ichitsubo, *Phys. Chem. Chem. Phys.* **2019**, *21*, 23749–23757 ; f) K. Ariyoshi, S. Masuda, *Phys. Chem. Chem. Phys.* **2020**, *22*, 4677–4684; g) A. Medina, A. Rodríguez, C. Pérez-Vicente, R. Alcántara, *Dalton Trans.* **2021**, *50*, 2123–2130; h) J. Han, S. Yagi, T. Ichitsubo, *J. Power Sources* **2019**, *435*, 226822–226829.

[8] a) K. Shimokawa, T. Ichitsubo, *Curr. Opin. Electrochem.* **2020**, *21*, 93–99; b) F. Tuerxun, S. Otani, K. Yamamoto, T. Matsunaga, H. Imai, T. Mandai, T. Watanabe, T. Uchiyama, K. Kanamura, Y. Uchimoto, *Chem. Mater.* **2021**, *33*, 1006–1012.

[9] G. S. Gautam, P. Canepa, A. Urban, S. H. Bo, G. Ceder, *Chem. Mater.* **2017**, *29*, 7918–7930.

[10] J. C. Knight, S. Therese, A. Manthiram, *J. Mater. Chem. A* **2015**, *3*, 21077–21082.

[11] J. Yin, A. B. Brady, E. S. Takeuchi, A. C. Marschilok, K. J. Takeuchi, *ChemmComm* **2017**, *53*, 3665–3668.

[12] a) Y. Zhang, G. Liu, C. Zhang, Q. Chi, T. Zhang, Y. Feng, K. Zhu, Y. Zhang, Q. Chen, D. Cao, *Chem. Eng. J.* **2020**, *392*, 123652–123661; b) A. Banu, A. Skakunthala, M. Thamilsselvan, P. S. Kumar, K. Suresh, S. Ashwini, *Ceram. Int.* **2019**, *45*, 13072–13085; c) R. Yokozaki, H. Kobayashi, T. Mandai, I. Honma, *J. Alloys Compd.* **2021**, *15*, 159723–159729.

[13] a) G. Vaish, R. Kripal, L. Kumar, *J. Mater. Electron.* **2019**, *30*, 16518–16526; b) A. Jain, S. P. Ong, G. Hautier, W. Chen, W. D. Richards, S. Dacek, S. Cholia, D. Gunter, D. Skinner, G. Ceder, K. A. Persson, *APL Materials* **2013**, *1*, 011002-; c) S. M. Antao, I. Hassan, J. B. Parise, *Am. Mineral.* **2005**, *90*, 219–228.

[14] a) J. C. Hunter, *J. Solid State Chem.* **1981**, *39*, 142-; b) M. M. Thackeray, P. J. Johnson, L. A. Picciotto, P. G. Bruce, J. B. Goodenough, *Mat. Res. Bull.* **1984**, *19*, 179–187.

[15] C. B. Azzoni, M. C. Mozzati, L. Malavasi, P. Ghigna, G. Flor, *Solid State Commun.* **2001**, *119*, 591–595.

[16] a) S. Ivanova, E. Zhecheva, D. Nihtianova, M. Mladenov, R. Toyanova, *J. Alloys Compd.* **2013**, *561*, 252–261; b) M. G. Naseri, M. H. M. Ara, E. B. Saion, A. H. Shaari, *J. Magn. Magn. Mater.* **2014**, *350*, 141–147; c) V. A. Ivanshin, J. Deisenhofer, H. A. Krug von Nidda, A. Loidl, A. A. Mukhin, A. M. Balbashov, M. V. Bremin, *Phys. Rev. B* **2000**, *61*, 6213–6219.

[17] a) T. Brezesinski, J. Wang, J. Polleux, B. Dunn, S. H. Tolbert, *J. Am. Soc.* **2009**, *131*, 1802–1809; b) M. C. López, G. F. Ortiz, P. Lavela, R. Alcántara, J. L. Tirado, *ACS Sustainable Chem. Eng.* **2013**, *1*, 46–56; c) H. Wang, N. Mi, S. Sun, W. Zhang, S. Yao, *J. Alloys Compd.* **2021**, *15*, 159294–159302.

[18] S. J. Clark, M. D. Segall, C. J. Pickard, P. J. Hasnip, M. J. Probert, K. Refson, M. C. Payne, *Z. Kristallogr.* **2005**, *220*, 567–570.

[19] F. G. B. Ooms, M. Wagemaker, A. A. van Well, F. M. Mulder, E. M. Kelder, J. Schoonman, *Applied Physics A* **2002**, *74*, 1089–1091.

[20] H. Shasha, N. Yatom, M. Prill, J. Zaffran, S. Biswas, D. Aurbach, M. Caspary Toroker, Y. Ein-Eli, *J. Solid State Electrochem.* **2019**, *23*, 3209–3216.

Manuscript received: May 13, 2021
Accepted manuscript online: June 24, 2021
Version of record online: July 20, 2021

 © 2021 The Authors. Chemistry - A European Journal published by Wiley-VCH GmbH